

PROBING THE DARK FLOW SIGNAL IN *WMAP* 9-YEAR AND *PLANCK* COSMIC MICROWAVE BACKGROUND MAPS

F. ATRIO-BARANDELA¹, A. KASHLINSKY², H. EBELING³, D. J. FIXSEN⁴, AND D. KOCEVSKI⁵

¹Física Teórica, Universidad de Salamanca, E-37008 Salamanca, Spain; atrio@usal.es

²NASA Goddard Space Flight Center and SSAI, Observational Cosmology Lab, Greenbelt, MD 20771, USA; Alexander.Kashlinsky@nasa.gov

³Institute for Astronomy, University of Hawaii, Honolulu, HI 96822, USA; ebeling@ifa.hawaii.edu

⁴NASA Goddard Space Flight Center and UMCP, Observational Cosmology Lab, Greenbelt, MD 20771, USA; Dale.Fixsen@nasa.gov

⁵Physics and Astronomy, 5800 Mayflower Hill, Waterville, ME 04901, USA; dale.kocevski@colby.edu

Received 2015 May 11; accepted 2015 July 18; published 2015 September 8

ABSTRACT

The “dark flow” dipole is a statistically significant dipole found at the position of galaxy clusters in filtered maps of Cosmic Microwave Background (CMB) temperature anisotropies. The dipole measured in *WMAP* 3-, 5-, and 7-year data releases was (1) mutually consistent, (2) roughly aligned with the all-sky CMB dipole, and (3) correlated with clusters’ X-ray luminosities. We analyzed *WMAP* 9-year and *Planck* 1st-year data releases using a catalog of 980 clusters outside of the Kp0 mask to test our earlier findings. The dipoles measured on these new data sets are fully compatible with our earlier estimates, are similar in amplitude and direction to our previous results, and are in disagreement with the results of an earlier study by the Planck Collaboration. Furthermore, in the *Planck* data sets dipoles are found to be independent of frequency, ruling out the thermal Sunyaev–Zeldovich as the source of the effect. In the data of both *WMAP* and *Planck* we find a clear correlation between the dipole measured at the cluster location in filtered maps and the average anisotropy on the original maps, further proving that the dipole is associated with clusters. The dipole signal is dominated by the most massive clusters, with a statistical significance that is better than 99%, slightly larger than in *WMAP*. Since both data sets differ in foreground contributions, instrumental noise, and other systematics, the agreement between the *WMAP* and *Planck* dipoles argues against them being due to systematic effects in either of the experiments.

Key words: cosmic background radiation – cosmology: observations – galaxies: clusters: general – large-scale structure of the universe

1. INTRODUCTION

Measurements of peculiar velocities with galaxies rely on distance indicators to subtract the Hubble expansion and have achieved notable success in probing peculiar velocities using galaxy surveys out to $\leq 100 h^{-1}$ Mpc (e.g., see the review by Strauss & Willick 1995). However, individual galaxy distance indicator surveys are typically restricted to isolated parts of the sky, which should then be corrected for when reconstructing galaxy flow characteristics, such as the amplitude of the bulk flow on a given scale (e.g., Watkins et al. 2009). SN Ia surveys input highly accurately measured individual distances (Turnbull et al. 2012), but are sparse and require corrections for sky coverage effects (Rathaus et al. 2013). More critically, in all such measurements the galaxy velocity is probed with respect to the frame of the Hubble expansion and translated into the cosmic microwave background (CMB) rest-frame after assuming that the entire CMB dipole is of a purely kinematic origin, caused by the Doppler effect due to the local motion of our Galaxy, Local Group, etc. (Kogut et al. 1993, but also see the discussion of Wiltshire et al. 2013).

The kinematic Sunyaev–Zel’dovich (KSZ; Sunyaev & Zel’dovich 1972) directly measures the peculiar velocity of clusters with respect to the CMB and does not require the subtraction of the velocity due to the Hubble expansion. Therefore KSZ offers an alternative method for probing a peculiar velocity field at larger distances that are potentially inaccessible to galaxy distance indicator methodologies. Its main disadvantage is that the temperature fluctuations due to the peculiar motion of individual clusters are much smaller than the cosmological CMB signal, foreground emissions,

instrumental noise, or the thermal Sunyaev–Zeldovich anisotropies (TSZ; Sunyaev & Zel’dovich 1970) from the thermal motion of electrons in the potential well of clusters. As a result, the peculiar velocity of a single cluster has yet to be determined. Kashlinsky & Atrio-Barandela (2000, hereafter KA-B) thus proposed a method for probing the bulk motion of clusters of galaxies, collectively using all-sky CMB maps combined with an all-sky X-ray cluster catalog. They pointed out that one can construct a statistic, the dipole moment evaluated at cluster locations over a fixed aperture containing the entire X-ray emitting gas, that can probe the bulk flow down to cosmologically interesting levels for the *WMAP* and *Planck* instrumental configurations. The KA-B method requires filtering out the primary CMB component *without removing the KSZ signal*, and isolating the TSZ contribution to the measured dipole. For the former, KA-B proposed a variant of the Wiener filter, designed to minimize the contribution from the primary CMB with the known mean power spectrum, whereas the TSZ component can be attenuated if the gas X-ray temperature, T_X , decreases toward the outer parts in clusters, as was indeed empirically discovered (Atrio-Barandela et al. 2008).

The KA-B method was first applied to the 3-year *WMAP* CMB data coupled with an extended cluster catalog where, surprisingly, a statistically significant dipole over the cluster apertures containing zero monopoles was found for a volume of median/mean depth of $\sim 300 h^{-1}$ Mpc (Kashlinsky et al. 2008, 2009, hereafter KABKE, KABKE2). Within the statistical and systematic calibration uncertainties this corresponded to the cluster sample moving at $\sim 600\text{--}1000$ km s⁻¹ in the direction of the CMB dipole. KABKE termed this the “dark flow,” speculating that it may be reflective of the *effective*

motion across the entire cosmological horizon. If true, this is equivalent to at least a part of the all-sky CMB dipole being of primordial origin, a possibility that requires an isocurvature component in the primordial density field (Matzner 1980; Turner 1991; Mersini-Houghton & Holman 2009). Using a further expanded cluster catalog and *WMAP* 5-year CMB maps Kashlinsky et al. (2010, hereafter KAEEK) showed that the cluster dipole correlated with cluster properties, increasing in amplitude for the most X-ray luminous and massive clusters, as expected from SZ contributions (the TSZ contribution was small over the final apertures, as evidenced by the zero monopole there). Atrio-Barandela et al. (2010, hereafter AKEKE) have developed—analytically and numerically—the formalism to understand the error budget of the **KA-B** method, which can and should be applied to any such measurement as a consistency check.⁶ Kashlinsky et al. (2011, hereafter KAE11) have shown that the results can be probed with public cluster data, which they have posted for interested investigators at www.kashlinsky.info/bulkflows/data_public. The methodology of the analysis, the results, and their potential implications have been extensively reviewed in Kashlinsky et al. (2012, hereafter KAE12).

Motivated by the final *WMAP* 9-year and *Planck* 1-year data releases we have scrutinized our previous “dark flow” measurements with the further developed methodology and present the results here. We do not address our interpretation of the signal here: throughout we refer to the statistically significant dipole remaining at cluster positions and with an amplitude that correlates with X-ray cluster luminosity pointing as the “dark flow signal,” within the uncertainties, in the direction of the all-sky CMB dipole. Because *WMAP* does not have the frequency coverage required to distinguish a KSZ dipole from the dipole generated by a random distribution of the TSZ anisotropy, we evaluated the final dipoles at apertures containing zero monopole. Since the mean TSZ monopole is an upper bound on the TSZ generated dipole, this aperture guarantees that the measured dipole was not due to the TSZ effect. Importantly, *Planck* has measured on both sides of the zero-TSZ frequency at 217 GHz and has provided the appropriate data to test whether the dipole contains a significant TSZ contribution. For this data we just require the aperture to be large enough for the errors to integrate down and leave a statistically significant dipole. We will show that at the same aperture the *Planck*-based results are fully consistent with those of *WMAP*, providing a very important consistency check. The measured dipole turns out to be independent of frequency and is consistent with the CMB blackbody energy spectrum and therefore cannot be due to TSZ or foreground residuals since those components vary with frequency.

We find the same results as before with the *WMAP* 9-year data analysis, but given the lower noise levels of that data set and the new methodology here we can isolate the signal better. We then apply the methodology to the *Planck* 1-year data and we find full consistency with the *WMAP* results. There appears to be a statistically significant “dark flow” signal at cluster locations with the dipole amplitude that correlates with cluster X-ray luminosity and the direction pointing within the uncertainties to the direction of the all-sky CMB dipole. If

the measured signal with all its properties can arise from something other than KSZ, we would welcome this discussion.

This paper is structured as follows: for completeness we briefly revisit the methodology, the data processing pipeline, and the error budget of the **KA-B** measurement. Then in Section 3 we present the analysis of the *WMAP* 9-year data, which empirically supports the error budget estimations derived in Section 2 and our previous measurements. Section 4 addresses our measurement of the dark flow signal with the *Planck* 1-year data. We find full consistency between the *WMAP* and *Planck* results, except that for the map at 30 GHz and in particular cluster configurations, which could be affected by low-level systematics, consistent with the effects of striping due to the *Planck* observing strategy. The “dark flow” measured in *Planck* is significant at better than the 99% confidence level. When combined with the fact that the signal correlates with cluster X-ray luminosity and points in the direction of the all-sky CMB dipole, the significance of the existence of the primordial contribution to the CMB dipole, known as “dark flow,” is even larger. Throughout this paper we use the X-ray cluster catalog compiled for the KAEEK study. A more advanced and expanded catalog is now being worked on and upon its completion we will present the results from its application.

2. METHODOLOGY, DATA PROCESSING, AND ERROR BUDGET

2.1. *KA-B* Method

A cluster in the direction \hat{n} , moving with a peculiar velocity \mathbf{v} , will generate a temperature anisotropy $\Delta T_{\text{KSZ}} = -T_0 \tau (\mathbf{v} \cdot \hat{n}/c)$, where τ is the projected electron density along the line of sight, c is the speed of light, and T_0 is the CMB blackbody temperature. A sample of clusters randomly located in the sky and moving with an average velocity of \mathbf{V}_{bulk} will produce a temperature anisotropy $\Delta T_{\text{KSZ}} = -T_0 \tau (V_{\text{bulk}}/c) \cos \theta$, where θ is the angle with respect to the apex of the motion. At the position of clusters, microwave temperature anisotropies have several components: primary CMB, TSZ, and KSZ components, foreground residuals, and instrument noise. **KA-B** estimated how these terms integrated down with many clusters, concluding that at the resolutions of the *WMAP* and *Planck* channels, the dominant contribution to the noise of the KSZ measurement would be from primary CMB anisotropies. **KA-B** proposed using the known statistical properties of the primary CMB to filter out this contribution and increase the signal-to-noise of the probed KSZ term. The **KA-B** proposed filter minimizes the difference $\langle (\Delta T - \mathcal{N})^2 \rangle$, with \mathcal{N} being the instrumental noise (Kashlinsky et al. 2009). **AKEKE** have shown analytically and numerically that it effectively removes the primary CMB signal down to the cosmic variance (CV). In ℓ -space the **KA-B** filter is $F_\ell = (C_\ell^{\text{sky}} - C_\ell^{\text{th}} B_\ell^2) / C_\ell^{\text{sky}}$, where C_ℓ^{sky} is the actual realization of the radiation power spectrum in *our sky* that includes noise, TSZ, KSZ, foreground residuals, and primary CMB; C_ℓ^{th} is the power spectrum of the Λ CDM model realization that best fits the data, and B_ℓ is the antenna beam.

2.2. Data Processing Pipeline

WMAP and *Planck* have measured the microwave sky at different frequencies with varying angular resolutions. We implement our filter, taking into account the specifics of each of

⁶ As we will discuss later and as was pointed out numerous times, Keisler (2009) claims errors that violate the **AKEKE** analytical and numerical evaluations and are indicative of an error that he confirmed in private correspondence.

the *WMAP* Differencing Assembly (DA) and *Planck* channels. Our pipeline for measuring the dark flow signal works as follows.

1. We start with foreground-cleaned all-sky microwave maps.
2. The data of each channel are multiplied by the Galactic and point source mask. To facilitate comparison with our previous results we chose the *WMAP* Kp0 mask.
3. Next, the monopole, dipole, and quadrupole are subtracted from the regions outside the mask. Then we compute the multipole expansion coefficients $a_{\ell m}$ correcting for the mask.
4. The $a_{\ell m}$ coefficients are multiplied by the filter F_{ℓ} before transforming them back into real space to create the filtered map. Since the quadrupole and octopole are aligned with the dipole the filter is set to zero for $\ell \leq 3$ to avoid any cross-talk between those scales that could mimic a dipole.
5. The monopole and dipole outside the mask are removed from the filtered maps.
6. The dipoles are computed at the cluster positions using a fixed aperture for all clusters for a given depth and, X-ray luminosity bin.

Our first results, presented in Atrio-Barandela et al. (2008) and KABKE1 and 2, were obtained using different apertures. We estimated the size of the region that emitted 99% of the X-ray flux, θ_x , for each cluster and computed dipoles in units of θ_x . The results were found to be very similar to those using a fixed aperture zero monopole for all clusters, so we present the results using fixed apertures where errors are simpler to compute and can be evaluated by analytic means providing multiple cross-checks (AKEKE).

As indicated in the introduction, KAEK showed that when binned by cluster X-ray luminosity, the cluster dipole measured in filtered maps correlated with central TSZ anisotropy in unfiltered maps, with larger amplitudes corresponding to the most X-ray luminous clusters, as expected from SZ contributions. Due to the inhomogeneous distribution of clusters on the sky, the mean TSZ anisotropy (or monopole) could generate a significant dipole and/or other higher order multipoles. It is important to demonstrate that the measured dipole was not due to the TSZ effect. *WMAP* operated in the Rayleigh–Jeans CMB regime and did not provide enough direct information to subtract the TSZ contributions from the measured dipoles. To ensure that in *WMAP* data the measured dipole was not dominated by the TSZ monopole we used the fact that all TSZ multipoles due to the inhomogeneous distribution of clusters on the sky, including the dipole, would be bounded from above by the monopole. Then, in step [6] we repeated the measurement for different apertures and selected the dipole measured at the *zero monopole* aperture to ensure that the TSZ component did not contribute to the measurement. This aperture is no longer necessary when using *Planck* data, where the TSZ vanishes at 217 GHz and any dipole there will be free from TSZ contributions.

2.3. Error Budget

We compute errors numerically using the same configurations and apertures that were used to evaluate the dipole at the cluster positions in KAEK. In KAE12 we discussed four different methods to evaluate numerically the errors and

showed their mutual consistency (Section 10.3). Our dipole is measured at cluster pixels so the error on this measurement is determined by the distribution of the random dipoles in the data away from the actual clusters. We evaluate these random dipoles by placing filled aperture disks at random positions in the sky with the same angular extent as was used to measure the dipole at the cluster location. We remove all pixels within 80 arcmin from the center of all known clusters to make sure that the randomly distributed disks do not overlap with them. By using the realization of the primary CMB as given by the actual sky to measure the dipole and its error we take into account the effect of all possible systematics existing in the filtered data, such as foreground residuals, inhomogeneous and correlated instrument noise, as well as any artifact that could have been introduced by our pipeline like mode coupling and power leakage between the galactic mask and the cosmological signal remaining in the filtered data. In Atrio-Barandela (2013) we discussed the different biases and inefficiencies that exist between different types of simulations that can result on overestimating the errors. In AKEKE we developed an analytical insight to detail the different contributions to the error bars and their properties when the instrumental noise is Gaussian-distributed and foreground residuals are negligible. More details are given in AKEKE and KAE12 (Section 10.3), where it is shown that numerical simulations of the actual CMB sky give errors that are in excellent agreement with the analytical theory. This formalism clarifies the relation between the errors of the monopole and of the three dipole components and their scaling with the number of clusters; this formalism is briefly summarized below.

The filtered maps have variance $\sigma_{\text{fil}}^2 = (1/4\pi)\sum(2\ell + 1)F_{\ell}^2 C_{\ell}^{\text{sky}}$. While the filter erases a large fraction of the primary CMB anisotropy, it leaves a residual due to cosmic variance (CV) that is common to all frequencies. The realization of the radiation power spectrum as seen from our location, C_{ℓ}^{sky} , differs from the underlying power spectrum C_{ℓ}^{th} by a random variable of zero mean and (cosmic) variance $\Delta_{\ell} = (\ell + \frac{1}{2})C_{\ell}^{\text{th}}/f_{\text{sky}}$ (Abbott & Wise 1984). In addition, the instrument noise is also present with a power spectrum N_{ℓ} . Neglecting foreground residuals in the foreground-cleaned maps, AKEKE have demonstrated that the variance of the filtered map is given by propagating the CV (see Section 10.3.1 of KAE12 for a more detailed derivation)

$$\sigma_{\text{fil}}^2 = \frac{1}{4\pi}\sum(2\ell + 1)\left[\frac{\Delta_{\ell}}{C_{\ell}^{\text{th}} + \Delta_{\ell} + N_{\ell}} + \frac{N_{\ell}}{C_{\ell}^{\text{th}} + \Delta_{\ell} + N_{\ell}}\right] = \sigma_{\text{CV,fil}}^2 + \sigma_{N,\text{fil}}^2(t_{\text{obs}}). \quad (1)$$

This expression is valid in the limit of zero-TSZ contribution and thus does not reflect the fact that the final errors will depend on the radius of the aperture chosen around each cluster, so they need to be computed numerically. An error-aperture dependence is to be expected since the residual CMB and noise have different spectra as shown in AKEKE (see Figure 1); the residual cosmological CMB signal dominated at $\ell \leq 300$ while the noise dominated at $\ell \geq 300$. By taking larger apertures the instrument noise integrates down and the residual CMB dominates the error budget. For this reason the final errors on *WMAP* and *Planck* will be similar even if they have

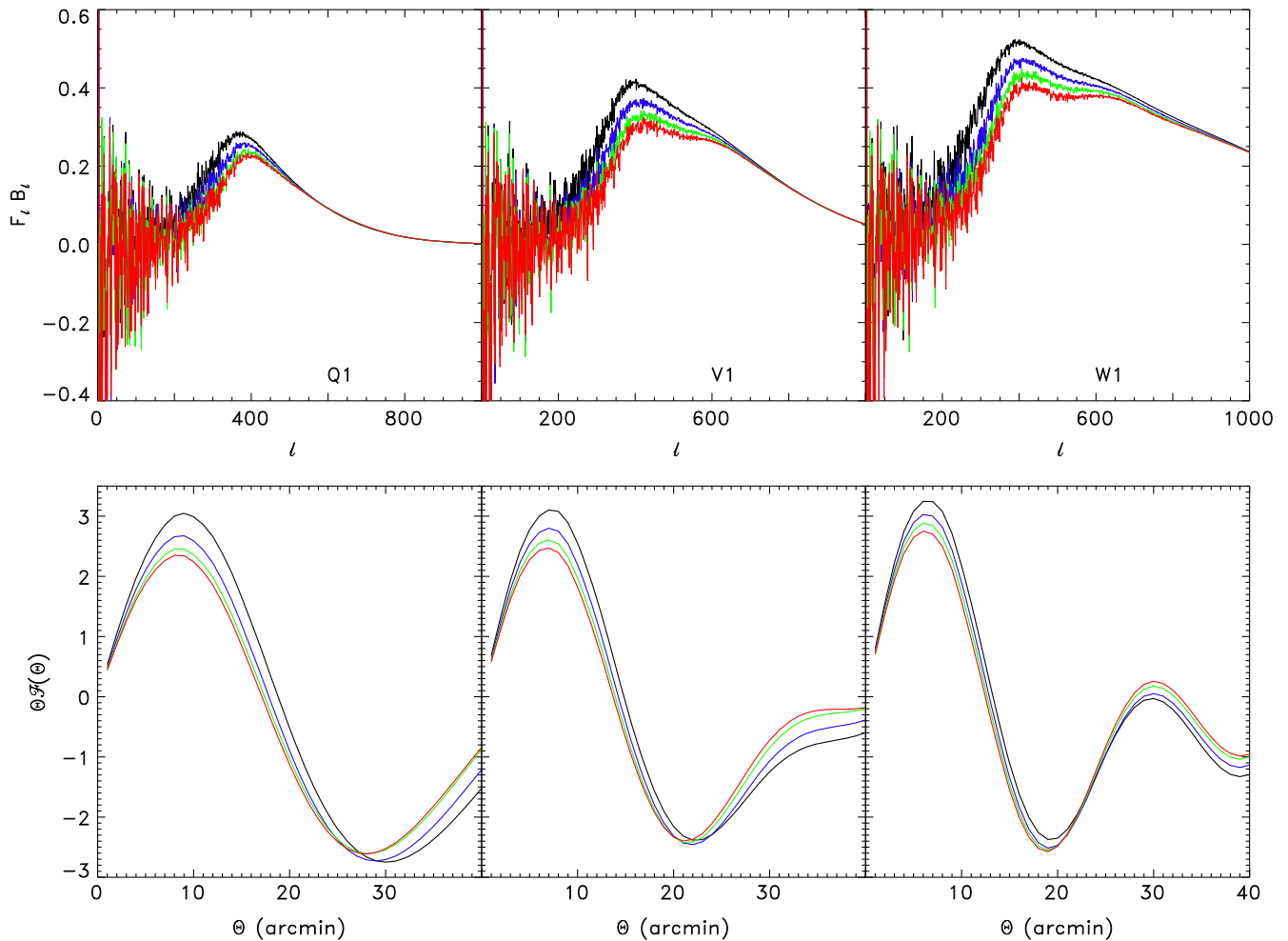


Figure 1. Wiener filters constructed with the 3-, 5-, 7-, and 9-year data (and noise levels). The top panels correspond to the filter in l -space and the bottom panels correspond to the same filters in real space. In each panel, the black, blue, green, and red curves from top to bottom correspond to the 3–9-year data. The galactic mask used was the *WMAP* Kp0 mask.

very different noise levels. For *WMAP* we chose an aperture that guarantees that there are no contributions to the dipole due to the TSZ effect. At this aperture errors integrate down and leave a statistically significant dipole. Nevertheless, Equation (1) is very instructive since it shows that the variance of the filtered maps depends mainly on two components: (a) the residual CMB not removed by the filter due to CV and (b) the noise that decreases with increasing time of observation t_{obs} . Figure 1 of [AKEKE](#) demonstrates empirically the high accuracy of the above expression.

By construction, the filtered maps have no intrinsic monopole or dipole. Since we measure these two moments from a small fraction of the sky, our limited sampling generates an error due to the (random) distribution of these quantities around their mean zero value. This error is proportional to the rms dispersion of the filtered map, the size of the fixed aperture around each cluster, and the number of clusters N_{cl} of the catalog. For a fixed aperture, the cosmic variance term of Equation (1) scales as N_{cl}^{-1} while the noise term scales as $(N_{\text{cl}} N_{\text{pix}})^{-1}$, with as N_{pix} the number of pixels within a fixed aperture around each cluster. The sampling variances of the monopole and three components of the dipole (a_0 , a_{1m}) depend on how homogeneously clusters sample the sky. A direct

calculation shows that the monopole (σ_0) and three dipole (σ_m) errors are:

$$\sigma_0 \equiv \langle a_0^2 \rangle^{1/2} \approx \frac{\sigma_{\text{fil}}}{\sqrt{N_{\text{cl}}}}, \quad \sigma_m \equiv \langle a_{1m}^2 \rangle^{1/2} = \frac{\sigma_0}{\langle \hat{n}_i^2 \rangle}, \quad (2)$$

where \hat{n}_i are the clusters' direction cosines. If clusters were homogeneously distributed in the sky then $\langle \hat{n}_i^2 \rangle = 1/3$, and the errors on the dipoles would be related to that on the monopole as expected: $\sigma_m = \sqrt{3} \sigma_0$, since three quantities are evaluated from the same data as the monopole. As we will discuss in Section 3.2, this expression is only approximately true since, due to the galactic mask, the error on the X and Y components of the dipole is slightly larger than that of the Z component (see [AKEKE](#), Section 10.3.2 and Figure 10.7 of [KAE12](#) for a detailed discussion).

The analytical formalism summarized in this section neglects the contribution of possible foreground residuals but they are already included in the numerically computed statistical uncertainties, since, as mentioned above, we compute errors using the same realization of the sky than the data, therefore including foreground residuals as well as all other systematics. We find that Equations (1) and (2) agree with the errors found

in simulations from the actual sky, showing empirically that foreground contributions are small.

2.4. Filtering and Noise

The lower noise levels of *Planck* as compared with *WMAP*, as well as different and independent systematics, allow a second and in some ways independent measurement of the KSZ signal, providing further tests of our filtering scheme. The **KA-B** filter has been designed to remove the cosmological signal by minimizing the difference between the data and the instrumental noise, i.e., the filter minimizes $\langle(\Delta T - \mathcal{N})^2\rangle$. The filter oscillates around zero, $F_\ell \simeq 0$, where the noise is negligible and $F_\ell \simeq 1$ where the noise dominates. If the noise decreases, the filter will remove all signals down to the limit imposed by CV (**KABKE2**). Since CV decreases as $\ell^{-1/2}$, lowering the noise implies that the filter will remove the signal at high ℓ 's more effectively. Then, whether the TSZ and KSZ signals survive or not, our filtering will depend on how these contributions are distributed in ℓ -space. For instance, the average TSZ anisotropy when evaluated at the cluster locations is a monopole, and in the absence of mask, filtering will distribute it preferentially to even multipoles while the bulk flow due to all the clusters is a dipole and it will be distributed preferentially to odd multipoles. In other words, the filter depends on the instrument noise (see Section 2.1) and maps with the noise of different amplitudes will give different filtered maps; this will change the redistribution of the TSZ and KSZ components, and the intrinsic CMB and foreground residuals, changing the amplitude and direction of the measured dipole. Therefore, due to the difference in noise amplitude and properties, it is important to compare the results obtained with *WMAP* and *Planck* to isolate the effect of systematics.

3. THE DARK FLOW DIPOLE IN *WMAP* 9 YEAR DATA

We first present the results of our analysis of the dark flow signal in the final *WMAP* 9-year data. To facilitate the comparison with our earlier results, we use the Kp0 mask to remove the Galaxy and the X-ray cluster catalog assembled for the **KAEEK** study. This catalog contains 980 clusters outside of the *WMAP* Kp0 mask, with redshifts $z \leq 0.25$ and X-ray luminosities in the *ROSAT* (0.1–2.4) KeV band of $L_X \geq 0.2 \times 10^{44} \text{ erg s}^{-1}$. Of those, 598 have X-ray luminosities $L_X > 10^{44} \text{ erg s}^{-1}$. We consider four cumulative redshift bins, selecting clusters by redshift: $z \leq (0.12, 0.16, 0.2, 0.25)$. In each redshift bin, we define three independent cluster subsamples according to their luminosity. These subsamples are $L_X = (0.2\text{--}0.5, 0.5\text{--}1.0, > 1.0)$ (in the same units as before) for clusters with $z < 0.12$ and $L_X = (0.5\text{--}1.0, 1.0\text{--}2.0, > 2.0)$ for all other bins. The number of clusters and other properties of each subsample are given in Table 1 of **KAEEK**. In total we only have 11 different bins since the bins $z < 0.2$ and $z < 0.25$ with $L_X < 10^{44} \text{ erg s}^{-1}$ differ by two clusters and their results are almost identical.

3.1. *WMAP* Filtering and Results

In **KABKE**, **KAEEK**, and **KAE11** we have analyzed the subsequent data releases of *WMAP* 3-, 5-, and 7-year data, respectively. We have consistently constructed the filter from the same data that we used to compute the dipoles. With each release, the noise level in the map has decreased, changing the filter. Motivated by the discussion in the Section 2.4 we can

now test the robustness of the detected dipole signal with respect to the noise level of the filter, i.e., we can test the effect of the noise in redistributing the signal in the ℓ -space of the filtered maps and its effects on the measured dipole. For this purpose, we have constructed four filters for each of the eight single-frequency all-sky CMB maps using the data from the 3-, 5-, 7-, and 9-year releases. During these integrations the rms instrument noise has been reduced by a factor $\sqrt{3}$, so each subsequent filter would progressively remove a larger fraction of the intrinsic CMB signal. The four different filters were then applied to the *WMAP* 9-year data of the ultimate noise achieved with that instrument. The filters in multipole (top panels) and angular (bottom panels) space are shown in Figure 1, where one can also see the differences in the maps of different resolutions, ranging from Q at $\sim 30'$ to W at $12'$. Since the noise is largest at the W DAs and lowest at Q, more structure survives in the former than in the latter filter. However, combining the four W DAs decreases the instrument noise by a factor of 2.

The overall signal-to-noise ratio (S/N) of the **KAEEK** measurement is driven by the most luminous X-ray clusters, as it should be if the dipole arises from the SZ cluster components. In Figure 2 we show the dipole at the zero monopole aperture at the positions of the brightest clusters with $L_X \geq 2 \times 10^{44} \text{ erg s}^{-1}$ from Table 1 of **KAEEK**. The three panels correspond to different redshifts, as indicated. These bins contain 130, 208, and 322 clusters, respectively. Solid circles correspond to an averaging over all eight *WMAP* DAs (Q, V, W bands) and open circles to averaging over four W DA's that can resolve clusters better. The horizontal axis indicates the data used to construct the filter which is, as we have indicated above, always applied to the the *WMAP* 9 year data release. For the different filters, the zero monopole aperture changes from 20 to 30 arcmin depending on the chosen cluster sample. Nevertheless, the difference with the results at a fixed aperture, say 25 or 30 arcmin, is negligible since the residual monopole is always small, proving that the dipole is not contaminated by the TSZ monopole. The black line and shaded area correspond to the dipoles measured in **KAEEK**, obtained from *WMAP* 5-year data for the same cluster samples. The figure shows a reassuring consistency between the 9-year *WMAP* data (with any filter) with what was obtained in **KAEEK** for 5-year *WMAP* data, which in turn have been demonstrated to be consistent with 3- and 7-year *WMAP* CMB data in **KAEEK** and **KAE11**.

3.2. The Error Budget for *WMAP* Filtering

In **AKEKE**, **KAE12** we have discussed the proper methods for computing error bars and have addressed their relative merits and intrinsic biases. In Section 10.3.2 of **KAE12** we compared four alternative methods and showed that they all give similar uncertainties. As indicated in Section 2.3, we compute error bars by choosing random positions in the sky that were outside of the known clusters and the mask, and evaluating dipoles subtended by a given aperture around these centers, referred to as Method 1 in **KAE12**. Each run was done with several apertures and with different numbers of clusters, in the range of $100 < N_{\text{clus}} < 600$. We compute the monopole and dipole at those N_{clus} random positions using the *Healpix remove_dipole* routine. Our errors are the rms deviations of all those monopoles and dipoles, which coincide with the 68% confidence level for these demonstrably Gaussian distributions.

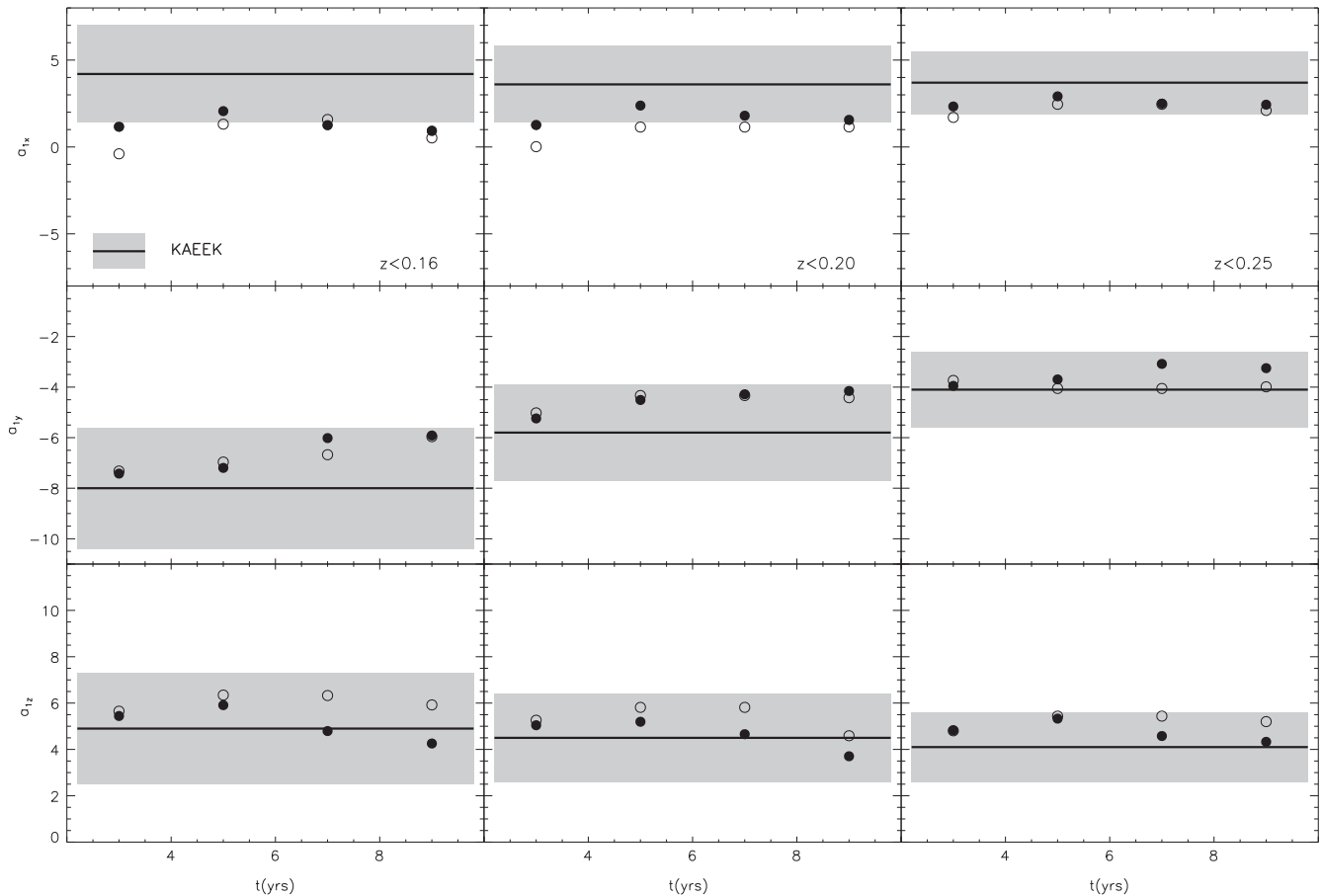


Figure 2. Dipoles measured in *WMAP* 9-year maps filtered with 3-, 5-, 7-, and 9-year noise filters for subsamples with $L_X \geq 2 \times 10^{44} \text{ erg s}^{-1}$ and the indicated redshifts. These bins contain 130, 208, and 322 clusters, respectively. Filled circles represent the averages over all 8 *WMAP* DAs; the open circles are the averages over the 4 *W*-band DAs. The solid lines and shaded regions correspond to the **KAEK** values and error bars.

As discussed in **AKEKE** and above, the dipole error budget is driven almost entirely by the error on the monopole, σ_0 , which should scale as $\propto N_{\text{clus}}^{-1/2}$. **AKEKE** have demonstrated, analytically and numerically, that the errors on the three dipole components should then be $\sigma_{1m} \simeq \sqrt{3} \sigma_0$ with $\sigma_{1x} > \sigma_{1y} > \sigma_{1z}$. The errors claimed by Keisler (2009) do not satisfy this and point to the flaw in his analysis, namely that his error budget is driven by the residual dipole outside the mask in the filtered map, which he failed to subtract prior to computing dipoles at random locations,⁷ as was demonstrated in **AKEKE**. The left panels of Figure 3 show with simulations that for the *WMAP* 9-year noise levels, one obtains with good accuracy that $\sigma_{1x} \simeq 1.8\sigma_0$, $\sigma_{1y} \simeq 1.55\sigma_0$, $\sigma_{1z} \simeq 1.4\sigma_0$, with a weak aperture dependence. This confirms explicitly that the entire error budget is contained in σ_0 .

The middle panels of Figure 3 show the results of simulated errors on σ_0 for various cluster configurations and the **KABKE** 3- and 5-year filters for the 30' aperture that correspond approximately to the zero monopole aperture. The solid circles correspond to the average of all of the 8 DAs. The panels demonstrate the accuracy of the scaling of $\sigma_0 \propto N_{\text{clus}}^{-1/2}$ or more explicitly $\sigma_0 \simeq 20N_{\text{clus}}^{-1/2} \mu\text{K}$, with a weak dependence on the selected filter, which is valid in the limit of the instrument noise

levels corresponding to 9-year *WMAP* and *Planck* data. This quantifies the errors explicitly.

The right panels of Figure 3 show the error on the monopole, $\sigma_0 \times N_{\text{clus}}^{1/2}$, as a function of the aperture radius when averaging over all 8 DAs (filled circles) and the 4 *W*-band DAs (open circles). This is compared with the component of Equation (1) that results from the CV of the primary CMB discussed in **AKEKE**, Section 10.3.1 of **KAE12**, and above, shown with a thick horizontal line. The three dipole components show a similar behavior, decreasing with increasing aperture radius as the noise integrates down, and are not shown. One can see explicitly that as the *WMAP* 9-year instrument noise decreased with increasing aperture, the monopole errors σ_0 approach this limit very accurately. Any filtering scheme should be able to evaluate similar expressions and then verify whether their particular claims are commensurate with this theoretically justified limit (see Planck Collaboration 2014g). The final zero monopole aperture at $\simeq 30'$ (**KABKE** and **KAEK**) is where the instrument noise (and foreground residuals) in the *WMAP* 9-year CMB maps contribute about $\sim 10\%$ to the total error, and so the latter is driven by CV from the primary CMB.

3.3. The “Dark Flow” Dipole from the *WMAP* Data

In **KAEK** we demonstrated that the measured dipole correlated with cluster X-ray luminosity binning. We selected clusters by their redshift and we divided the samples into three bins according to their X-ray luminosity, L_X . We showed that

⁷ It is unfortunate that despite this his claims are still occasionally cited at face value.

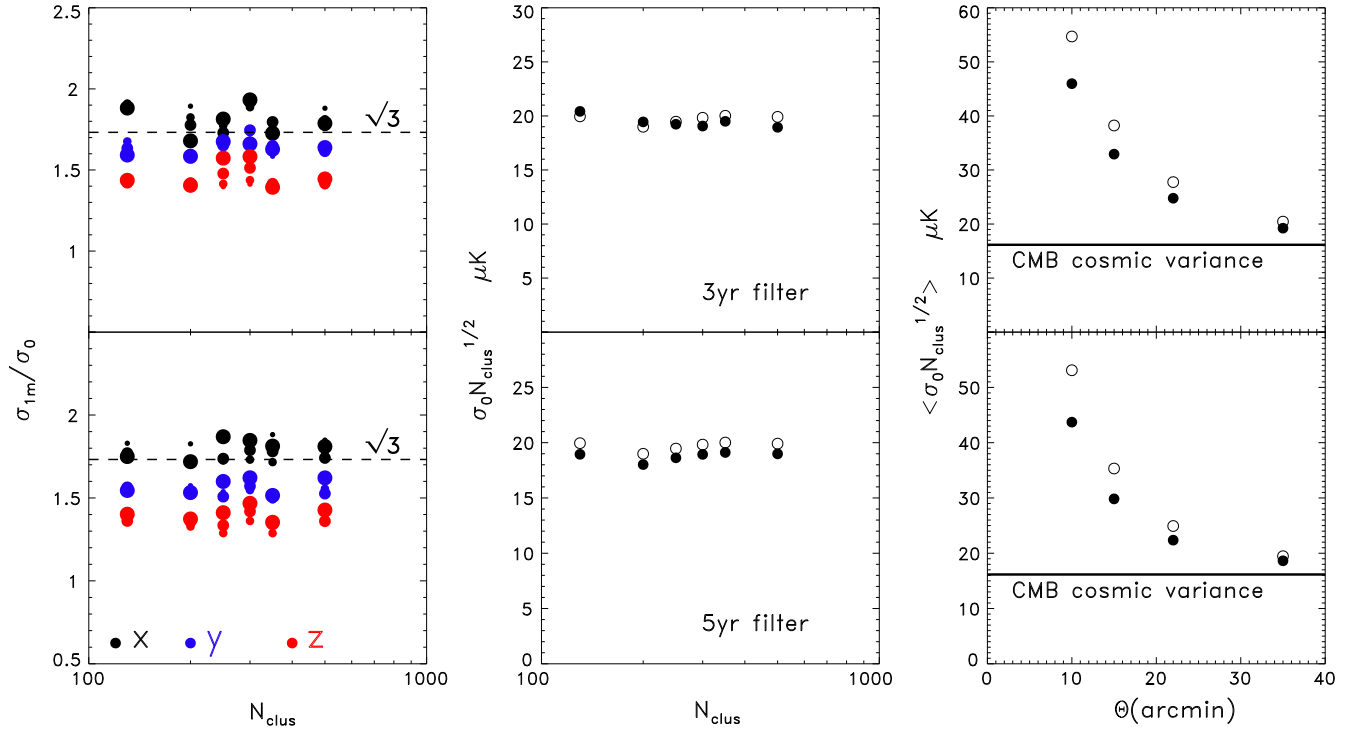


Figure 3. Error estimates. In the left panels the black, blue, and red circles correspond to the X , Y , and Z components of the error. Circles of increasing size correspond to apertures of $10'$, $15'$, $22'$, $35'$. The plot shows the robustness of the error estimates, driven predominantly by that of the monopole. The middle panels represent the monopole error vs. the number of clusters for Method 1 (see Section 3.2). Filled circles represent the average over all 8 DAs and open circles represent the average restricted to the 4 W -band DAs for apertures at $\sim 30'$. The errors show good accuracy with the analytical theory developed in [AKEKE](#) and [KAE12](#), Section 10.3. In the right panel we show the error vs. aperture with the same convention as in the middle panels. The thick horizontal line shows the zero noise cosmic variance limit $\sigma_{CV,fil}$ of the error (see Equation (1)).

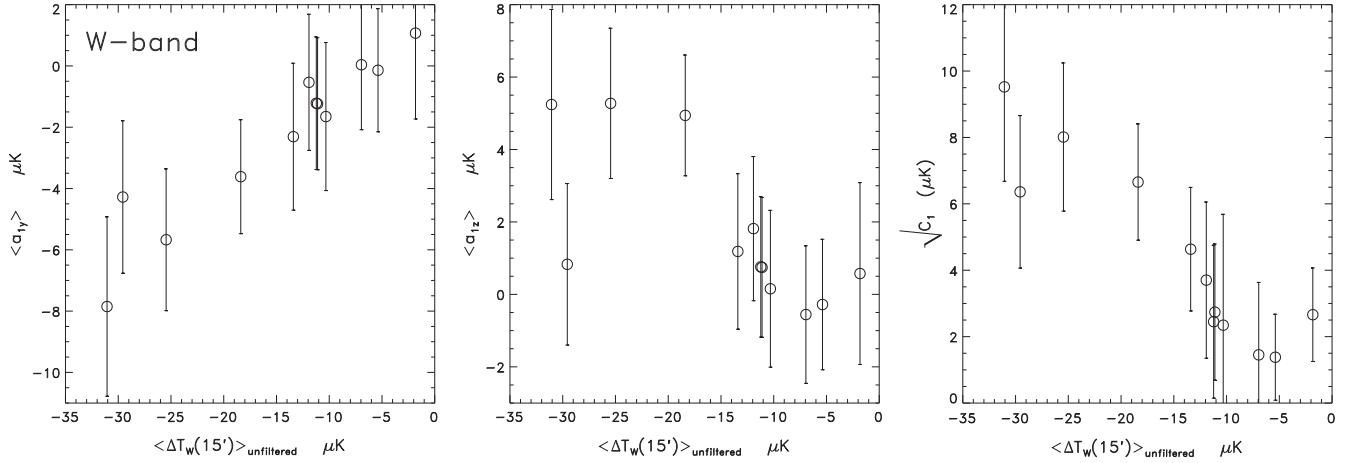


Figure 4. Results for W -band data per Table 1 of [KAEK](#) vs. the *unfiltered* central monopole. The dipoles were measured on an aperture of $30'$ radius and the errors have been computed using Method 1 (see Section 3.2).

clusters in the highest luminosity bin, with $L_X[0.1-2.4 \text{ KeV}] \geq 2 \times 10^{44} \text{ erg s}^{-1}$, had larger monopoles and larger dipoles than the other two bins. In fact, at the cluster locations, the Y component of the dipole in filtered maps was correlated with the average temperature anisotropy measured from the original *unfiltered* map. This average (or monopole) was always negative, as expected if the anisotropy is dominated by the TSZ effect. Since in CMB maps temperature anisotropies are convolved with the antenna the correlation was not directly established with cluster luminosity or mass. But as the TSZ effect scales with X-ray luminosity and cluster mass, this

correlation was a clear indication that both the monopole and dipole originated within clusters.

In Figure 4 we present the final results from the cluster catalog binned by L_X and z per Table 1 of [KAEK](#). We plot the results of the Y and Z dipole components, evaluated at the zero monopole aperture, versus the central monopole evaluated from *unfiltered* CMB maps. As in [KAEK](#), the central monopole was evaluated by averaging over the central $10'$ radius; we only used the four W DAs with appropriate angular resolution when averaging and we checked that adding the other DAs gives consistent results. We show, as previously, that we recover

statistically significant results for the Y and Z components; the X component is consistent with zero within the errors, but in any event it can be derived from the right panel showing the dipole power, C_1 . As in [KAEEK](#) the cluster configuration (discussed later for the *Planck* analysis) results in the value of a_{1y} , measured at about 3.3σ and the value of a_{1z} at $\simeq 2.5\sigma$, fully in agreement with Table 1 of [KAEEK](#). Figure 4 shows the same dipole–monopole correlation that was found in [KAEEK](#). When one accounts for the L_X correlation, the overall “dark flow” dipole reaches about $\simeq 4\sigma$ significance as discussed in [AKEKE](#). In addition, the “dark flow” dipole direction coincides with the all-sky dipole direction (after correction for the local motion as discussed in Kogut et al. 1993); the probability of this happening by chance with the current errors is $\sim 10^{-2}$. This argues for the same statistically significant signal pointing to the “dark flow” as in [KAEEK](#).

4. THE “DARK FLOW” DIPOLE IN PLANCK DATA

In 2013 March, the Planck Collaboration released nine *Planck* Nominal maps from the low and high-frequency instruments (LFI and HFI, respectively). LFI has measured the CMB sky at frequencies of 30, 44, and 70 GHz, while the HFI has covered the range 100, 143, 217, 353, 545, and 857 GHz (Planck Collaboration 2014a).⁸ These maps contain significant foreground contamination due to synchrotron and free–free emissions at low frequencies and thermal dust CO emission and zodiacal light at high frequencies. At the HFI frequencies, where zodiacal light contribution is more important, we use HFI maps with this contaminant removed (Planck Collaboration 2014d).

In addition, the Planck Collaboration released four different foreground-cleaned reconstructions of the CMB temperature anisotropies over a large fraction of the sky. These maps were produced using the data from nine *Planck* channels, without including any other external data set, by applying different component separation techniques. Together with the foreground-cleaned *Planck* nominal maps described below, we will analyze the spectral matching independent component analysis (SMICA) map, constructed from a linear combination in harmonic space of the nine single-frequency maps of different resolution. The weights of each frequency vary with multipole ℓ . In SMICA the temperature anisotropy was estimated over 97% of the sky. The remaining area of the image shown in Figure 5 is replaced with a constrained Gaussian realization (Planck Collaboration 2014d). The component analysis used to construct the map does not preserve the TSZ signal, so it cannot be used to test the monopole-dipole correlation shown in Figure 4.

The SMICA map has an angular resolution of 5 arcmin, but its harmonic content is cut off at $\ell > 4000$. The noise has an average rms of $\sim 17 \mu\text{K}$, with a highly inhomogeneous distribution (see Figure 15 of Planck Collaboration 2014a). The method under-subtracts thermal dust emission, but at high latitudes, in the region where the CMB reconstruction is statistically robust, residuals are below a few μK in amplitude. Compared with other reconstructions using different techniques, SMICA produces the map with the lowest level of

residuals and for this reason it will be the one we will be considering here.

4.1. Cleaning Planck Nominal Maps from Foreground Contributions

Planck Nominal maps contain foregrounds due to diffuse emissions from the Galaxy and compact sources. The Galactic foregrounds are the main contaminants on large angular scales. The main contributions are synchrotron, free–free, and anomalous microwave emission due to spinning dust grains, thermal dust emission, and emission from CO rotational lines. At small scales, extragalactic foregrounds from compact sources and unresolved emission from radio and infrared sources are the dominant contribution (Planck Collaboration 2014d). Foregrounds can be removed through component separation methods or by reconstructing the foreground fields and subtracting them. Component separation methods are usually employed to produce a clean map of CMB temperature anisotropies with very low foreground contamination at the expense of losing frequency information (Planck Collaboration 2014d; Bobin et al. 2013, 2014). The Planck Collaboration provides templates for correcting foreground emission at different frequencies and this will be the approach we will use here. A joint analysis of *IRAS* and *Planck*’s three highest frequency channels showed that dust varies strongly on small scales due to dust evolution, extinction, and local effects, particularly in high-contrast molecular regions. To correct the thermal dust emission we need to take into account its great variability and for this purpose use the *Planck* dust model that gives the three parameters that define the modified blackbody emission law (dust-grain temperature, emissivity index, and optical depth) at the reference frequency of 353 GHz (Planck Collaboration 2014c). The map of the thermal dust component is given at the same healpix resolution as the HFI data, $N_{\text{side}} = 2048$. To accurately estimate the contribution of this emission at each *Planck* frequency we evaluate the spectral model in each sky pixel and convolve it with the passband of each detector. We apply this color correction using the publicly available routine `hfi_color_correction`. Similarly, the synchrotron and free–free emissions are cleaned using the data on the amplitude of those contributions at 30 GHz and a spectral index to scale it to other frequencies at each pixel on the sky (Planck Collaboration 2013). The data is given with a resolution of $N_{\text{side}} = 256$ and is integrated with the frequency response at each band using the same routine mentioned before to produce the color correction needed to estimate the flux weighted in each band. The maps of the low-frequency and high-frequency foregrounds are subtracted from each frequency map.

The next step of the process is to clean the CO emission. This contribution is only important for the 100, 217, and 353 GHz channels due to the (1–0), (2–1), and (3–2) rotational transition lines. The Planck collaboration has made available three different types of CO correction maps (Planck Collaboration 2014e). Type 1 maps are too noisy to be of use for our purposes, so we use the Type 2 maps to clean the 100 and 217 GHz channels, the only ones for which the correction is available.

Our final foreground-cleaned maps from 30 to 353 GHz, together with SMICA, are shown in Figure 5. The data is plotted in the range $[-300, 300] \mu\text{K}$ to emphasize the differences in noise and foreground residuals. We work with a Healpix resolution of $N_{\text{side}} = 1024$ (Gorski et al. 2005). In all the maps there are some residuals of Galactic emission along the Galactic plane but outside the Galactic plane the signal is

⁸ All *Planck* data products have been downloaded from the *Planck* Legacy Archive found at http://www.sciops.esa.int/index.php?project=planck&page=Planck_Legacy_Archive.

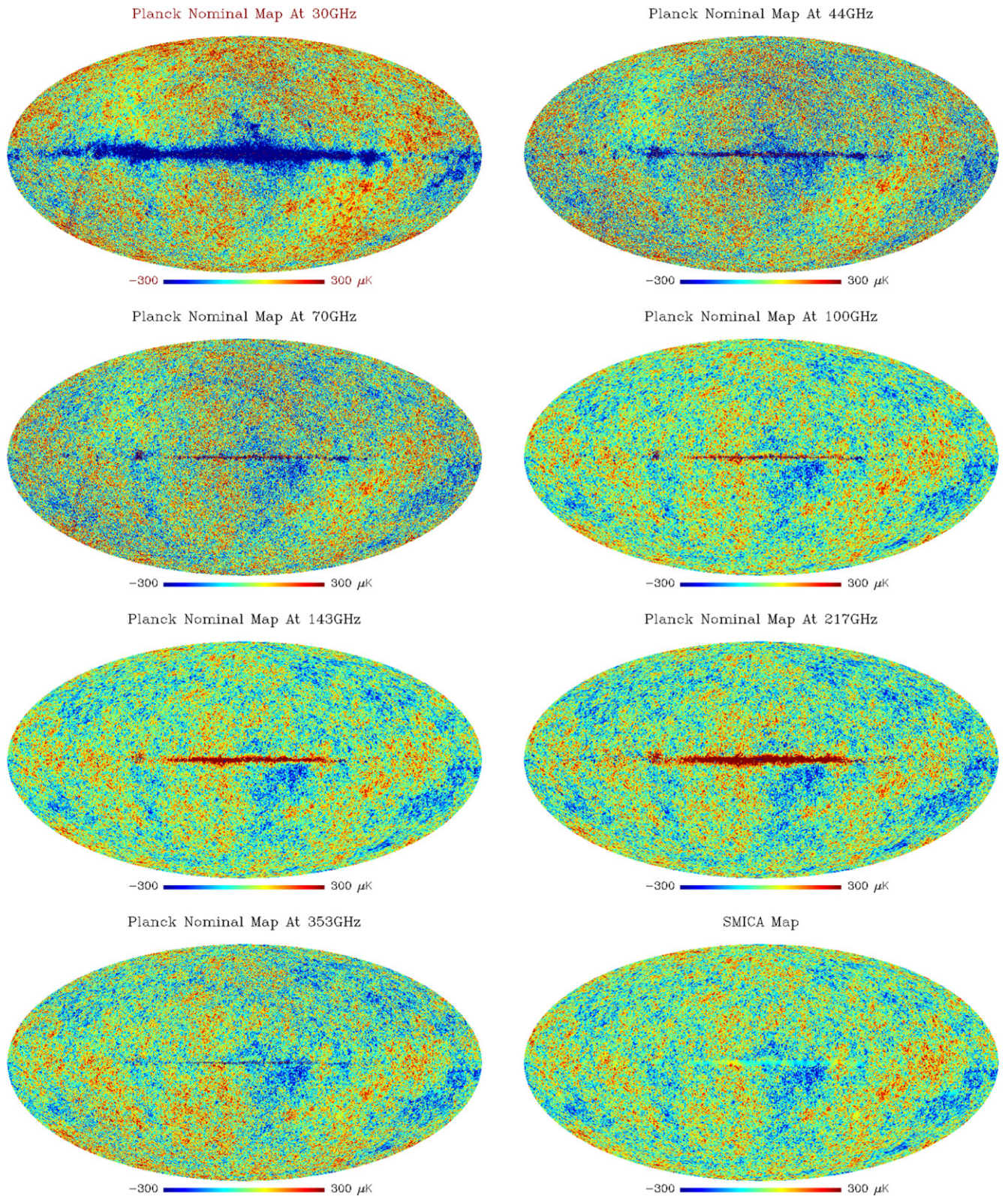


Figure 5. Foreground-cleaned *Planck* nominal maps. From top to bottom and left to right, maps correspond to channels of 30, 44, 70, 100, 143, 217, and 353 GHz; the bottom right plot corresponds to the SMICA CMB map.

clearly dominated by CMB fluctuations. We use the *WMAP* Kp0 mask to remove the regions around the Galactic plane and to reduce the contamination due to these foreground residuals as well as that of point sources. By using the same mask in *Planck* and *WMAP* we use the same fraction of the sky,

facilitating the comparison of the respective results. We did test that the COM-MASK-CMB union mask that removes 27% of the sky and is more adequate to the mask point source contribution from *Planck* data, gave the same results as those from the Kp0 mask. Note the stronger similarity of the HFI

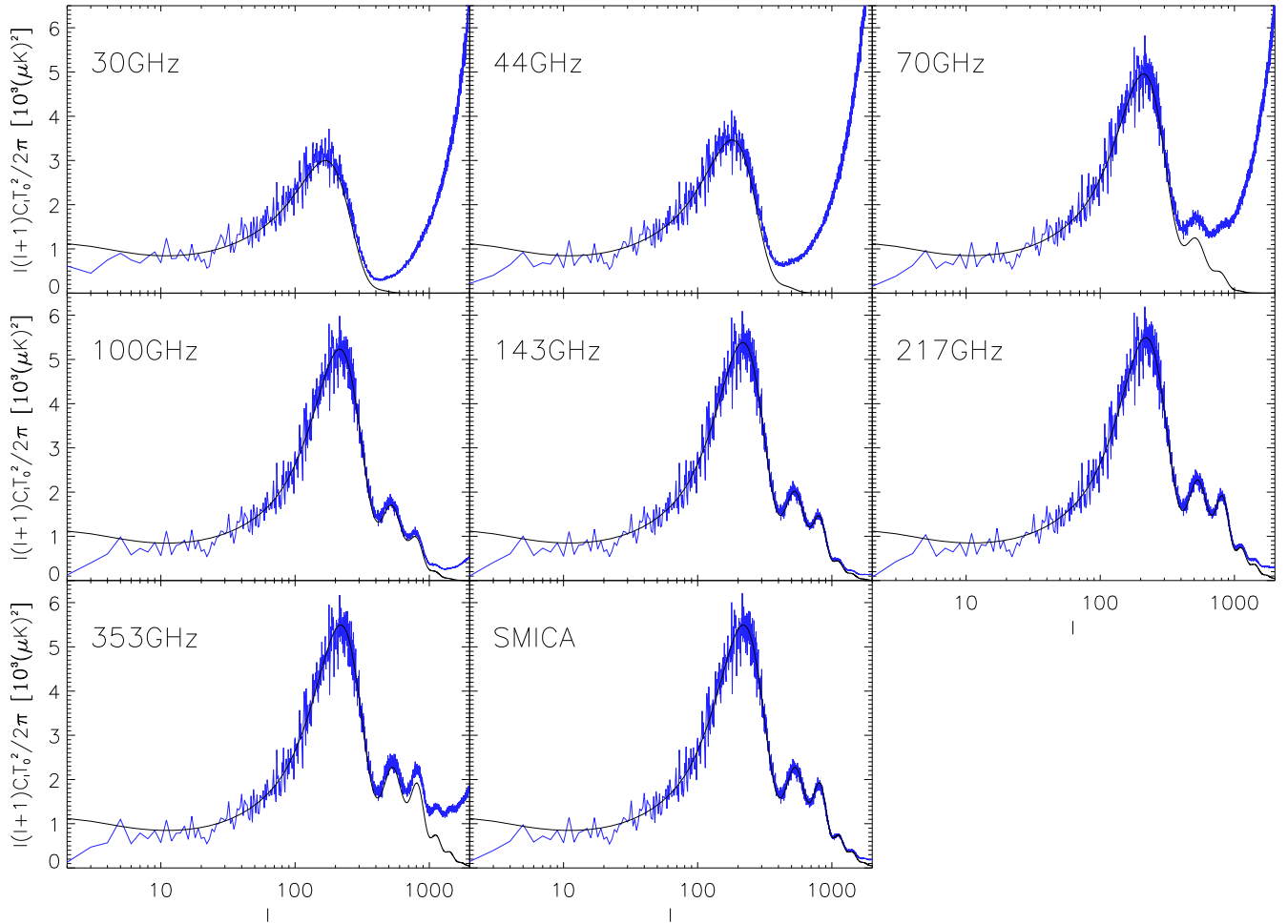


Figure 6. Radiation power spectra of the maps given in Figure 5. The blue and red lines correspond to the first and second frequencies specified in the text, respectively. The black lines correspond to the Λ CDM model that best fits the data, multiplied by a Gaussian beam at the resolution of each channel.

channels with the SMICA map, and the reconstruction of the intrinsic CMB anisotropies made by the Planck Collaboration, compared with the LFI channels. The 353 GHz map appears cleaner than the other HFI channels because it was at this frequency where the *Planck* dust model was evaluated. Dust residuals are larger at other frequencies due to the uncertainties in the modified blackbody model or in the determination of the emissivity index. The residual dust contamination in the Galactic plane diminishes at lower frequencies; at 44 and 70 GHz some residual synchrotron and free-free emission remains. Also, stripes associated with the *Planck* scanning strategy are clearly seen at 30 and 70 GHz. The satellite preferentially observes the sky at the ecliptic poles. Since the instrumental noise is higher at 30 and 44 GHz, the noise inhomogeneities due to this uneven sampling are clearly noticeable. We did not consider the maps at 545 and 857 GHz (not shown in Figure 5) due to their stronger foreground contamination that affected regions of high galactic latitude.

4.2. Planck Data Power Spectrum

The seven foreground clean maps of Figure 5 have an FWHM of approximately $\text{fwhm} = [33', 28', 13', 9'.7, 7'.3, 5', 5']$. Their power spectrum and the theoretical Λ CDM model, multiplied by the antenna beam, are represented in Figure 6 by a broken blue line and a smooth solid black line, respectively.

The region around the galactic plane was masked using the Kp0 mask to remove the foreground residual contributions near the galactic plane. The theoretical model fits the data rather well, with a flat spectrum, noise being the only other significant difference. In LFI the noise starts to dominate the intrinsic CMB signal at multipoles $l > 400-600$, as it is much smaller in HFI. In none of the spectra is there a deviation of the theoretical C_l 's due to foreground residuals or other artifacts, a reassuring fact that foregrounds have been removed to the levels required for this project.

4.3. Planck Data Systematics

The *Planck* satellite observed the sky at nearly great circles close to ecliptic meridians. The times a given position has been scanned (or “hit”) varies across the sky, giving rise to stripes with a similar pattern at ecliptic longitudes. The satellite produces one full sky map every 6 months; the initial and final position are matched with 6 months’ difference, when the instruments are looking in opposite directions in the solar system. Instrument noise, changes in gain, variations on the solar system foregrounds—mainly zodiacal light, and other effects contribute to small offsets between subsequent scans. As a result, the data shows stripes at nearly ecliptic meridians, most noticeably but not exclusively, at the 30 and 70 GHz channels.

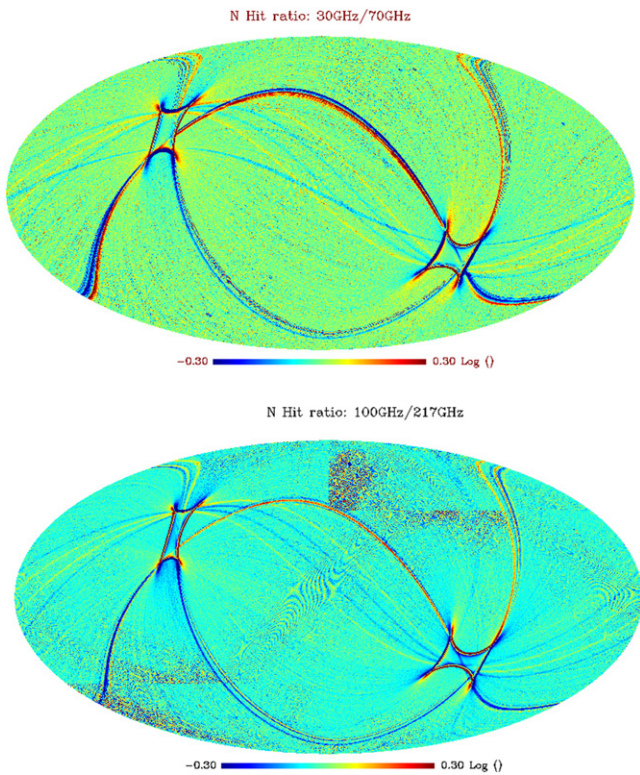


Figure 7. Ratio of the number of hits between the 30 and 70 GHz (left) and the 100 and 217 GHz channels (right). A blue stripe signifies that the number of hits of the 70, 217 GHz channels is larger than those of the 30, 100 GHz channels, and otherwise for a red stripe.

In Figure 7 we present the ratio of the hit maps of 30 and 70 GHz (left) and 100 and 217 GHz (right). Before taking the ratio, we divided each hit map by the mean number of observations to correct the differences between frequencies. Since the detectors at each frequency point to slightly different locations in the sky, the number of hits at a given location is different. A blue stripe in Figure 7 represents a scan where the number of hits on the 70, 217 GHz channels is larger than those on 30, 100 GHz, and a red stripe when it happens otherwise. If the sky coverage was uniform this ratio would be a constant. This figure demonstrates that even if in the foreground-cleaned maps of Figure 5 stripes are only seen in the LFI maps, they are also present at other frequencies. It would be important to precisely estimate the effects of the stripes on the noise. However, without access to the time-ordered data or the details of the systematic trends and details of which data came from which time we are unable to build a detailed covariance matrix. If there are residual effects from the stripes in the final data these should show up as differences when comparing to the *WMAP* data. The *WMAP* data has much stronger cross-linkages and so its stripes are smaller at higher spatial frequencies and less directional.

Finally, let us remark that the right panel of Figure 7 shows a band of a lower number of hits along the ecliptic plane and some rather odd features at $(l, b) = (0^\circ, 45^\circ)$ and at $(270^\circ, -45^\circ)$. We have no explanation about why data that has been taken along ecliptic coordinates would have been removed along Galactic parallels and meridians. Although we cannot estimate the effect of these noise inhomogeneities on the data, since we compute error bars using the filtered maps used to

compute the dipole, like in *WMAP*, they will be accounted for in our error bar estimates.

4.4. Results

WMAP and *Planck* scanning strategies are very different, so a comparison between both data sets is important for isolating systematics. To facilitate the comparison, we filter the CMB signal and compute the dipole at the cluster location following the same steps as in *WMAP*. We use the same mask in both data sets: the Kp0 mask. As the input theoretical model we use the Λ CDM radiation power spectrum with the *Planck* measured parameters. The filters of the seven *Planck* Nominal maps and the SMICA map are presented in Figure 8. The blue and red lines correspond to the first and second frequency indicated in each panel. Due to the higher noise levels in LFI channels, at $\ell \geq 500$ the filter is close to unity, while it oscillates around zero up to $\ell \simeq 10^3$ for the HFI channels and the SMICA map. Compared with the *WMAP* filters shown in Figure 1, the filters of the two lowest LFI frequencies are similar to those of *WMAP*, but the other filters are very different due to differences in resolution and instrument noise. This behavior can be explained by the functional form of our filter, $F_\ell = (C_\ell^{\text{sky}} - C_\ell^{\text{th}} B_\ell^2) / C_\ell^{\text{sky}}$; when the noise dominates $F_\ell \simeq 1$ and the graph of $F_\ell B_\ell$ behaves like B_ℓ . This is clearly seen in *WMAP* and the two lowest LFI frequencies at $\ell \geq 400$. When the noise is negligible, as in SMICA, then C_ℓ^{sky} differs from $C_\ell^{\text{th}} B_\ell^2$ due to CV, and F_ℓ oscillates around zero till the noise starts to dominate. For the maps with the lowest noise levels, this happens at higher values of ℓ . The exponential cutoff due to the antenna beam occurs at $\ell \sim 1500\text{--}2000$, almost outside the multipole range shown in Figure 8, giving the graph an overall different aspect. Therefore, with *Planck* data we can test the effect of the filter on our results more than we could with *WMAP*.

In Figure 9 we present the dipoles of the same three cluster configurations of Figure 2. Error bars were computed using Method 1: we generated 1000 templates of 800 disks randomly placed on the sky and computed the dipoles on the filtered maps of those random templates. For each template we took subsets of 100, 200, and 400 clusters and verified that $\sigma_{1m} \propto N_{\text{cl}}^{-1/2}$. As for *WMAP*, error bars on the dipole are driven by the error on the monopole and are approximately given by Equation (2).

The results presented in Figure 9 show a remarkable consistency among themselves and with those of *WMAP* 5-year data. The measured dipoles are *independent of frequency* (with the exception of 30 GHz) *and the filter* used. The filters, shown in Figure 8, have different structures in ℓ -space since they have been designed to remove the intrinsic CMB anisotropies attending to the specifics of each particular data set. Only the theoretical model C_ℓ^{th} is common to all filters. The consistency of the measured dipoles shows that our results are neither generated by artifacts introduced by our pipeline nor are dominated by systematics present on the data. The spectral distribution confirms our earlier findings with *WMAP*: The dipole cannot be due to the TSZ effect or from a systematic associated with foreground residuals in the data as the measured dipole remains constant at all frequencies except for the offset at 30 GHz, which is the most stripe-dominated. The dipole is clearly different from what it would be if it was due to the TSZ effect, as suggested by Osborne et al. (2011). In this case, the dipole had to be zero at 217 GHz and have the

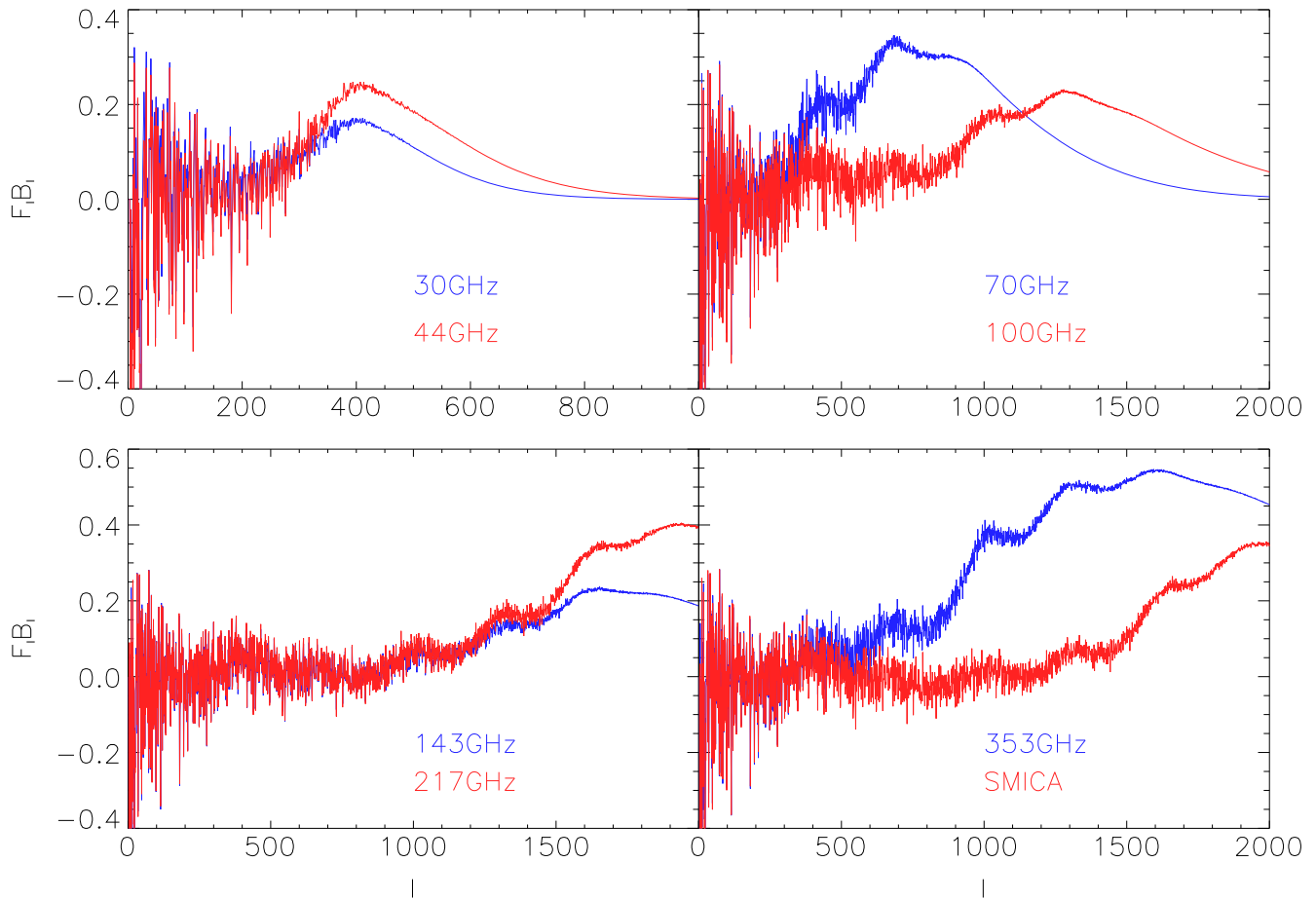


Figure 8. Filters in l -space of the seven foreground-cleaned *Planck* and SMICA maps. The lines follow the same convention as in Figure 6.

opposite sign at 353 GHz, none of which is observed. It is also different from what it would be if it was due to foreground residuals that correlated with cluster properties. All known foregrounds vary with frequency, contrary to what is shown in Figure 9, where the dipoles between 40 and 353 GHz remain constant, independent of frequency. Only the dipoles measured in the filtered 30 GHz map appear to be systematically different (at the $\sim 1\sigma$ level) and closer to zero than those of all the other maps, including the SMICA map. At the other *Planck* frequencies the dipoles are slightly offset compared with the values measured in *WMAP*. For example, at $z \leq 0.25$ a_{1Y} is systematically above the **KAEEK** value at more than 1σ . We will later discuss the possible reasons for systematic differences between *WMAP* and *Planck* results.

As in Figure 4, the dipoles measured in *Planck* data show a clear correlation with the TSZ monopole in the unfiltered map, both in the LFI and the HFI channels. In Figure 10 we show the dipole components, a_{1Y} and a_{1Z} , the dipole modulus, and the statistical significance for the cluster configurations selected according to redshifts $z \leq 0.16$, 0.2, and 0.25, and X-ray luminosities (in units of 10^{44} erg s^{-1}) in the range $L_X < 1$, $L_X = [1-2]$ and $L_X > 2$. The dipoles are plotted versus the monopole a_0 measured over a solid aperture of radius 10 arcmin in the original (unfiltered) foreground-cleaned *Planck* Nominal maps. For simplicity we only show two frequencies: 70 GHz (solid black circles) and 143 GHz (blue squares). The statistical significance has been computed by generating 10^5 random dipoles with zero mean and rms

dispersion for the uncertainty in each dipole component for each cluster configuration, and finding the fraction of random dipoles with amplitude larger than the measured value. The statistical significance exceeds 99% in the three most significant bins, the three bins with the brightest clusters, $L_X > 2 \times 10^{44}$ erg s^{-1} .

First, notice that at 70 GHz monopoles are larger than those at 143 GHz, but the ratio is smaller than ~ 1.7 , i.e., it is smaller than the ratio of the TSZ amplitude at 70–143 GHz. The 70 GHz channel has a lower resolution (see Section 4.2) and dilutes cluster anisotropies more than 143 GHz. Second, the largest monopoles and dipoles correspond to the most luminous 130 clusters with $z < 0.16$ but the highest significance corresponds to the 208 clusters with $z < 0.2$. The second bin has a larger number of clusters and the dipole components are measured with a slightly better S/N. This small difference results in great variations on the statistical significance since we are exploring the tail of the distribution.

4.5. Comparison of *WMAP* and *Planck* Dipoles

The dipoles measured at the different *Planck* frequencies display remarkable consistency, except for 30 GHz, and exhibit a strong correlation with the TSZ monopole. These results are consistent with the dipoles measured previously in *WMAP*. In Figure 11 we compare the three components of the dipole for the three X-ray luminosity bins of clusters with redshift $z \leq 0.16$ measured in *WMAP* 5-, 9-year data, and *Planck* data at 100 GHz, represented by triangles (red), diamonds (blue), and

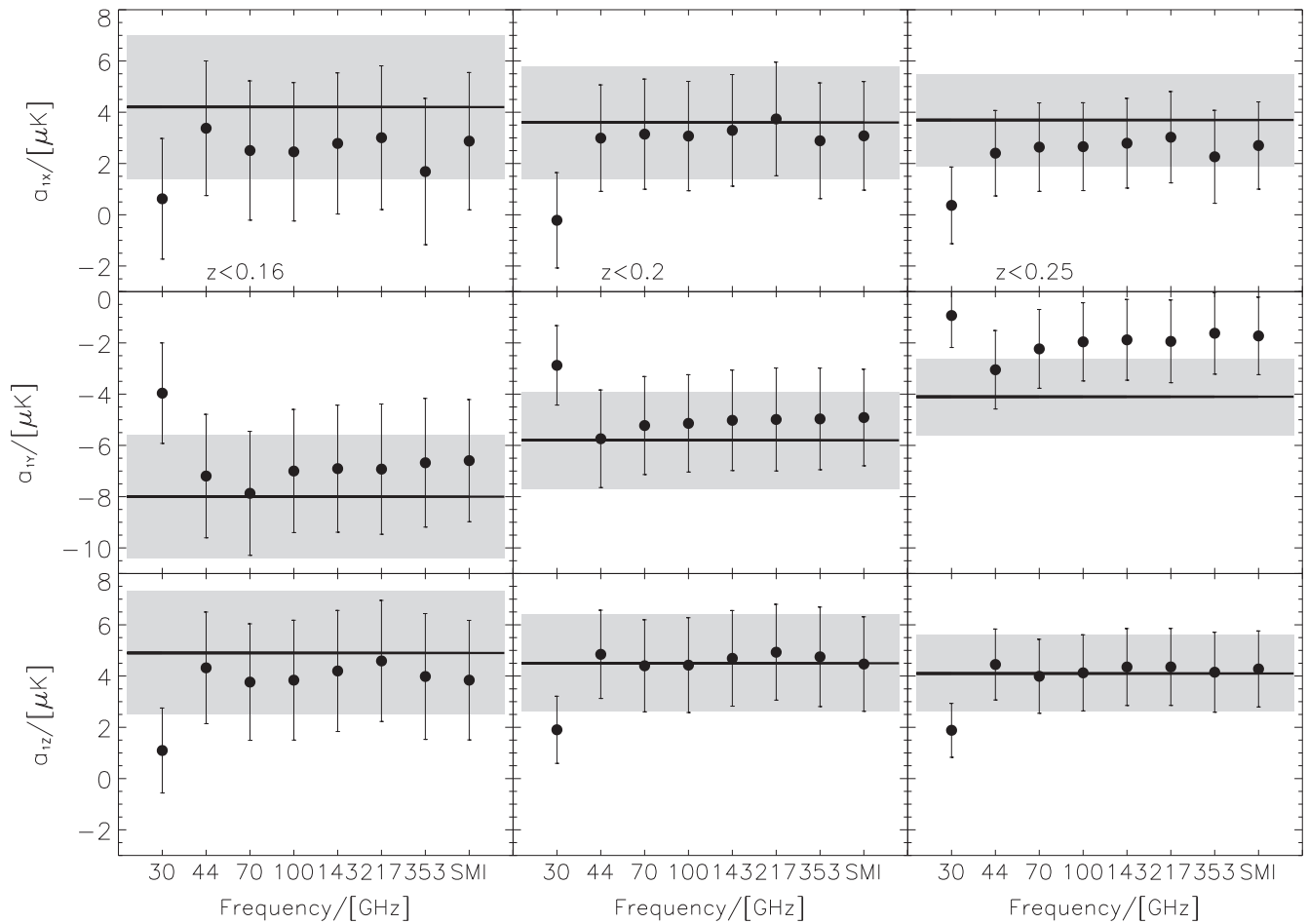


Figure 9. Comparison of *WMAP* 5-year and *Planck* 1-year dipoles. *Planck* dipoles are represented by filled circles, with the corresponding error bars computed using Method 1 (see Section 3.2). The solid lines and shaded areas correspond to the measured dipoles in *WMAP* 5-year data for the same cluster configurations, as in Figure 2.

solid circles (black), respectively. On the x-axis, the 5-year data is shifted by two units to avoid overplotting data. The results from *WMAP* 3- and 7-year data are also consistent with those plotted in the figure but are not shown to avoid overcrowding. The monopoles are computed on apertures of 10 arcmin in unfiltered maps while dipoles are computed over apertures of 25 arcmin radii, which correspond to the *WMAP* zero monopole aperture. Although the *WMAP* W-band frequency of observation is 94 GHz, not far from the 100 GHz channel shown in the figure, its monopoles are significantly smaller, particularly for the bin containing the most luminous clusters. The difference is due to *WMAP* having lower angular resolutions ($\sim 12'$) than *Planck* ($\sim 5'$) at those frequencies, and consequently the TSZ cluster anisotropy is more diluted.

While *WMAP* and *Planck* data are consistent, the data show some small but systematic differences. In Figure 12 we compare the dipoles of *WMAP* 9-year data, averaged over the 4 DAs of the W-band with the dipoles measured in *Planck* 70 GHz map, of similar angular resolution. Only 11 points (out of the 12 cluster subsamples of KAEK) are seen since two values merge on the plot, as indicated in Section 3. For reference, the red dashed line shows the dipoles as having the same value in both data sets. For clarity we do not show the error bars here; for any cluster subsample the dipoles of either satellite differ by less than one standard deviation. Figure 12 shows that the a_{1x} 's components are randomly distributed

above and below the red dashed line, the a_{1y} 's measured in *Planck* are systematically smaller than those of *WMAP* and the distribution of the a_{1z} 's is indifferent.

Although the discrepancies in Figure 12 are not yet relevant, the systematic offset in the Y component of the dipole or the discrepant results of the 30 GHz channel could be the result of systematics present in the *Planck* data. We have already noted in Figures 5 and 7 that foreground-cleaned *Planck* nominal maps contain very strong non-Gaussian features. Even if stripes correspond to differences in the number of observations (or weights) in the data, they are not erased but are rather enhanced by filtering. The filter depends on the noise; $(1/f)$ -features could introduce some effect, mostly in the 30 GHz map, the channel with the largest intrinsic noise of all the *Planck* frequencies. There are other effects that could be more pernicious. The low weight stripes are often there because over most of the sky there are 2 distinct sets of observations that are 6 months apart while at the beginning or end of the period there is only one set of observations. This has several effects. First, because there is only one set of data, there is a single correction for long term drifts so whatever effects there are, one has fewer data sets to average over. This increases the systematic effects according to the number of data sets, which is a small number. Second, there are fewer data to check these long term drifts against other data. Finally, in the middle of a data set one can interpolate, while at the end one must

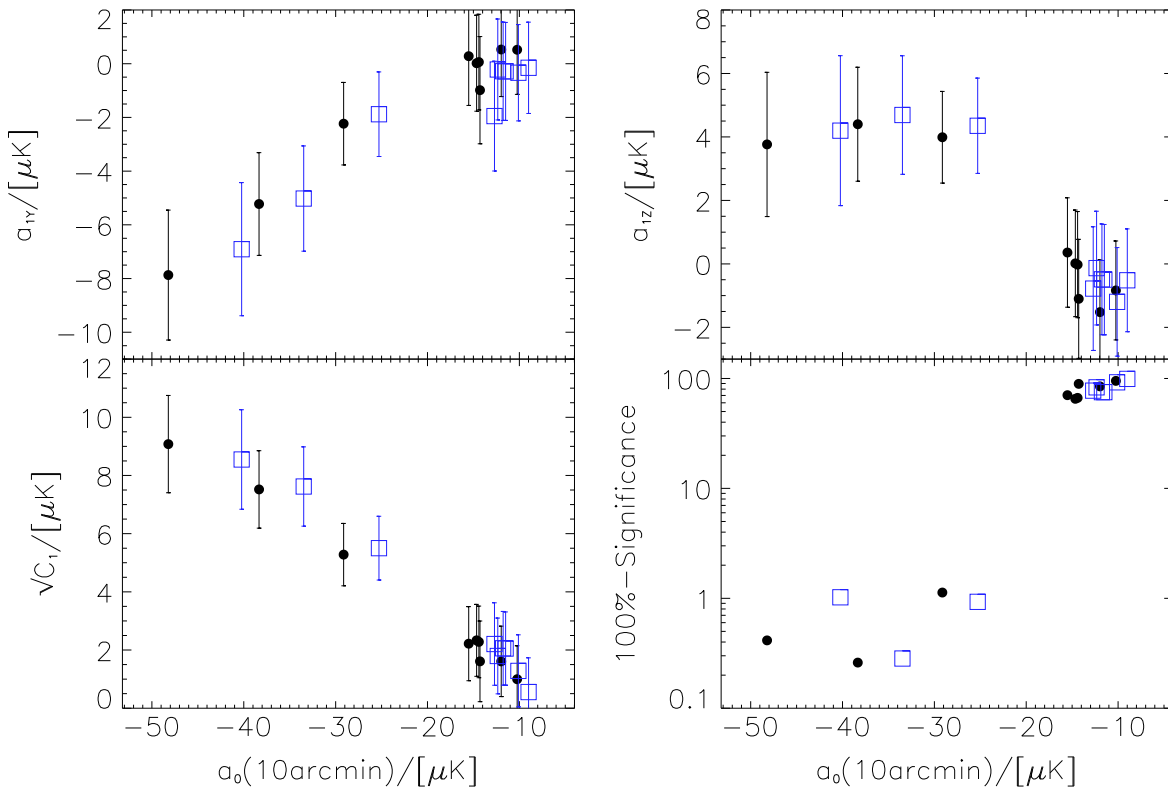


Figure 10. Dipoles for all the cluster configurations measured on apertures of $25'$ vs. the unfiltered monopole on $10'$ and their statistical significance. Error bars have been computed using Method 1. Only two channels are shown: 70 GHz (black solid circles) and 143 GHz (blue squares).

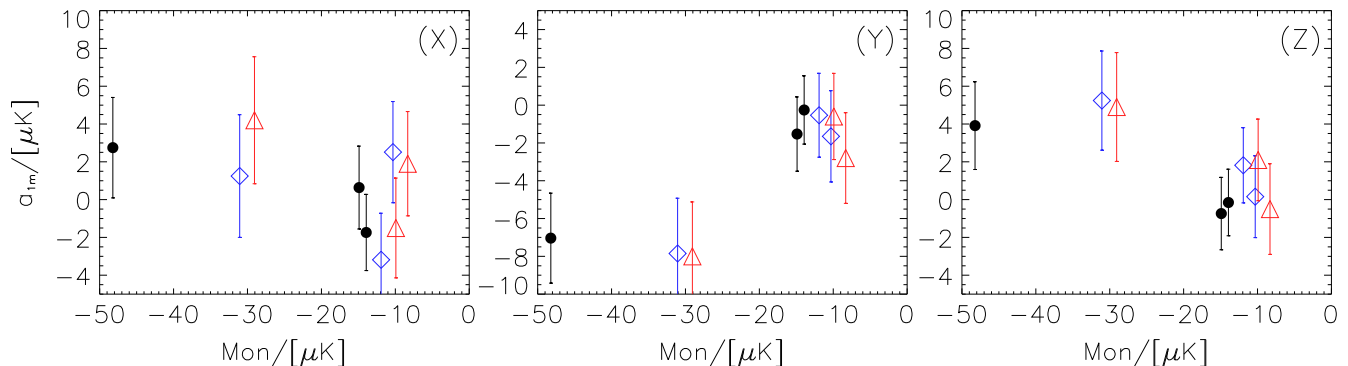


Figure 11. Comparison of *WMAP* and *Planck* dipoles for the three luminosity bins with of clusters with redshift $z \leq 0.16$. Triangles (red), diamonds (blue), and solid circles correspond to *WMAP* W-band 5-, 9-year data, and *Planck* data, respectively.

necessarily extrapolate, which is inherently more uncertain. These effects lead to higher noise at low frequencies. The pattern of the *Planck* observations puts the low temporal frequencies at low spatial frequencies. As can be noted from Figure 11 of Planck Collaboration (2014b) systematic effects have higher than proportional noise at low frequencies and this effect would be largest at 30 GHz, where the noise is higher, than at other channels and could be the underlying reason why the dipole has not been equally preserved by the filter than in *WMAP*. As indicated in Section 4.3, understanding the effect of stripes would require analyzing the time-ordered data and goes beyond the scope of this paper.

4.6. Comparison with *Planck* Earlier Results

Our results differ markedly from an earlier analysis of *Planck* data using the internal linear combination map (Planck

Collaboration 2014g, hereafter PIR-13), a foreground-cleaned map similar to SMICA that was constructed to measure the KSZ effect. The TSZ contribution in their map was removed to less than a few percent of its original value. The Planck Collaboration claims to not to have found any detection of a bulk flow as measured in any comoving sphere extending to the maximum redshift covered by their cluster sample. In fact, they found a dipole for their full cluster sample (see Figure 10 of PIR-13) that was similar to ours but overestimated their error bars, diluting the statistical significance of their measurement. The Planck Collaboration used two flawed methods to compute errors. (1) They rotated the cluster template around the z -axis; this method underestimates the error on the Z component and overestimates it in the X and Y components, giving an overall increment on the error of modulus (see Atrio-Barandela 2013, Table 1 and Figures 2 and 3). (2) They computed the errors

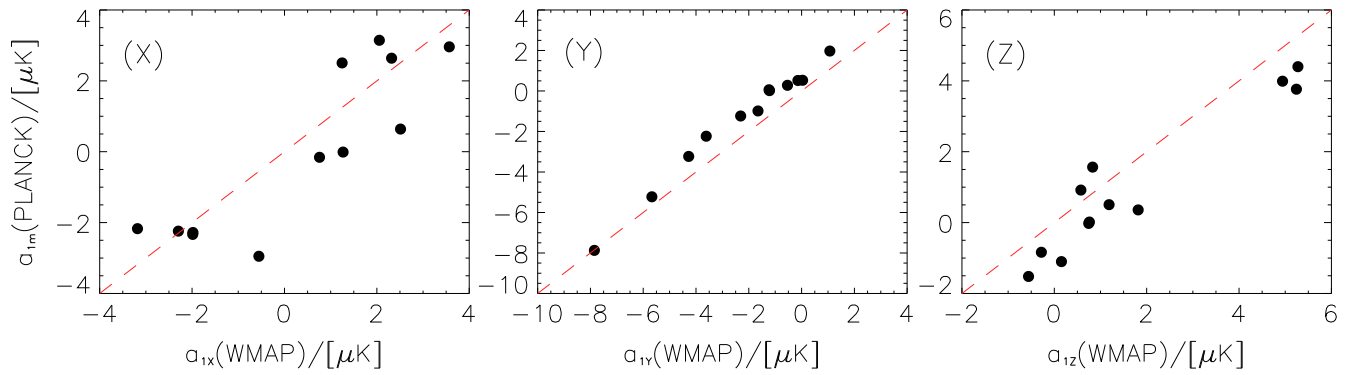


Figure 12. Comparison of the three dipole components measured in *WMAP* 9-year *W*-band data with those of *Planck* at 70 GHz for the same cluster subsamples. The dashed red line corresponds to the dipoles as being equal. For clarity, error bars are not shown. The differences between both data sets are always smaller than 1σ for all configurations.

measuring dipoles with the actual distribution of clusters over simulated CMB skies, but their simulations did not mimic the data accurately enough. In the real sky, filtering leaks power from high galactic latitudes to the Galactic plane. In their simulated maps the Planck Collaboration did not apply any galactic mask, preventing the power leakage to the plane of the Galaxy. As a result, their simulated maps contain higher power than the actual sky (see Atrio-Barandela (2013) Figures 4 and 5), again overestimating their errors by a similar amount as in their rotation method⁹ (see Atrio-Barandela 2013 for a full discussion). In addition, they did not find a larger dipole for their 200 most massive clusters. While some differences may arise from the differences in cluster samples, the lack of correlation between the dipole and monopole is probably due (A) to their binning and (B) to having eliminated the TSZ component from their map, a component which we have shown not to have an effect on the measured dipole (see Figure 9). In Figures 4 and 10 we have demonstrated that the largest dipole originates from clusters with $L_X > 2 \times 10^{44} \text{ erg s}^{-1}$ and $z < 0.16$. Adding clusters with higher redshift in the same luminosity bin reduces both the monopole and dipole, consistent with clusters being more diluted by the antenna. If their subsample of massive clusters is, on average, at higher redshifts, then their dipole should be smaller than the values we have found. To verify the dipole–monopole correlation they ought to have measured the TSZ from foreground-cleaned maps at different frequencies, to check if their most massive clusters produced the largest TSZ monopole or not.

5. CONCLUSIONS

We have computed the dipole at the cluster locations using the same techniques for *WMAP* and *Planck*. We find a “dark flow” signal that correlates with X-ray properties, and is therefore likely related to cluster gas, and not to the primary CMB, foregrounds, or noise. The results are in excellent agreement with our earlier findings and are consistent both in *WMAP* 9-year and in *Planck* 1-year data/ Those instruments used different scanning strategies, which resulted in different systematics and, while small differences remain, the close agreement is reassuring of the real nature of the dipole signal. Specifically we found the following.

1. The dipole at the zero monopole aperture remains at cluster positions at the same level as in [KAEK](#).
2. The dipole at cluster positions correlates with the TSZ monopole, a proxy for X-ray luminosity.
3. The signal is consistent among the different multi-year *WMAP* integration filters and with all *Planck* frequencies, except for a small, typically $\sim 1\sigma$, offset at 30 GHz.
4. The noise of the measurement in our filtered maps is in good agreement with the analytical and numerical theory developed in [AKEKE](#) and summarized here.
5. The overall statistical significance of the dipole signal in *WMAP* is similar to that found in [KAEK](#), and is larger for *Planck* than for *WMAP*.
6. Within the uncertainties the signal points in the direction of the all-sky CMB dipole.
7. If one accepts the KSZ interpretation of the detected statistically significant signal the equivalent velocity is $\sim 600\text{--}1000 \text{ km s}^{-1}$, which is within the systematic and statistical calibration uncertainties discussed by Kashlinsky et al. (2009), [KAEK](#), and Atrio-Barandela et al. (2012).

While we deliberately avoid interpretation here, we note that the measurements are consistent with the “dark flow” proposition ([KABKE](#)), namely the existence of a primordial CMB dipole of non-kinematic origin, which then presents itself as an effective motion across the entire cosmological horizon. No other alternative interpretation of the measured signal has been advanced, although it would be of scientific interest. Instead, the debate concentrated along the lines of trying alternative filtering schemes, which may erase the signal (Atrio-Barandela et al. 2012). Indeed, an all-sky filtering cannot imprint a dipole exclusively at cluster positions, which would in addition correlate with cluster X-ray luminosity, but given the still limited significance of the measurement of about $(3\text{--}4)\sigma$, other filtering schemes can reduce the measurement below being statistically significant (see Figure 13 of Osborne et al. 2011, where such alternative filtering schemes start picking up the KSZ signal at velocities exceeding $4000\text{--}6000 \text{ km s}^{-1}$).

If the “dark flow” corresponds to a large-scale motion it is of interest to compare with peculiar velocities derived using other methods. First, Planck Collaboration (2014f) have measured the aberration of the CMB temperature fluctuations due to our local motion, constraining the amplitude of large-scale flows in the direction of the solar motion, i.e., constraining the motion

⁹ This information was passed on by F.A.B. when the Planck Collaboration paper (2014g) was being written.

of the local group projected in that direction but not the full vector. Velocity estimates relying on distance indicators are affected by their uncertainties. For instance, Watkins & Feldman (2014) argue that their previous results overestimated the flow due to their distances being underestimated by 10%. Probes of the velocity field on scales of $\geq 100 h^{-1}$ Mpc depend on the value of the Hubble constant and the current discrepancies between local measurements and the *Planck* value make these measurements even more uncertain. SNe Ia have also been used to measure velocities. Turnbull et al. (2012) find that their sample does not show large-scale bulk flow. However, Wiltshire et al. (2013) argue for the opposite, finding that the Hubble expansion exhibits considerably more variance in the rest-frame of the CMB dipole than in the inertial frame of the local group. The cosmic radio dipole is also peculiar. It has an amplitude that is larger than expected from a purely kinematic effect and a significant contribution to this excess could come from a local void or similar structure Rubert et al. (2014). Future work, including work by our team that uses an expanded cluster catalog and is now in an advanced stage of preparation, should shed more light on the existence of the “dark flow.”

F.A.B. acknowledges financial support from the Spanish Ministerio de Educación y Ciencia (grant FIS2012-30926). We thank R. Génova-Santos for providing the foreground-cleaned maps used in this work.

REFERENCES

- Abbott, L. F., & Wise, M. B. 1984, *ApJL*, **282**, L47
- Atrio-Barandela, F. 2013, *A&A*, **557**, 116
- Atrio-Barandela, F., Kashlinsky, A., Ebeling, H., Kocevski, D., & Edge, A. 2010, *ApJ*, **719**, 77
- Atrio-Barandela, F., Kashlinsky, A., Kocevski, D., & Ebeling, H. 2008, *ApJL*, **675**, L57
- Atrio-Barandela, F., Kashlinsky, A., Kocevski, D., & Ebeling, H. 2012, arXiv:1211.4345
- Bobin, J., Starck, J.-L., Sureau, F., & Basak, S. 2013, *A&A*, **550**, 73
- Bobin, J., Sureau, F., Starck, J.-L., Basak, S., & Paykari, P. 2014, *A&A*, **536**, 105
- Gorski, K.M., Hivon, E., Banday, A.J., et al. 2005, *ApJ*, **622**, 759
- Kashlinsky, A., & Atrio-Barandela, F. 2000, *ApJL*, **536**, L67
- Kashlinsky, A., Atrio-Barandela, F., & Ebeling, H. 2011, *ApJ*, **732**, 1
- Kashlinsky, A., Atrio-Barandela, F., & Ebeling, H. 2012, PhR, commissioned/ submitted (arXiv:1202.0717)
- Kashlinsky, A., Atrio-Barandela, F., Ebeling, H., Edge, A., & Kocevski, D. 2010, *ApJL*, **712**, L81
- Kashlinsky, A., Atrio-Barandela, F., Kocevski, D., & Ebeling, H. 2008, *ApJL*, **686**, L49
- Kashlinsky, A., Atrio-Barandela, F., Kocevski, D., & Ebeling, H. 2009, *ApJ*, **691**, 1479
- Keisler, R. 2009, *ApJL*, **707**, L42
- Kogut, A., Lineweaver, C., Smoot, G.F., et al. 1993, *ApJ*, **419**, 1
- Matzner, R. 1980, *ApJ*, **241**, 851
- Mersini-Houghton, L., & Holman, R. 2009, *JCAP*, **2**, 6
- Osborne, S. J., Mak, D. S. Y., Church, S. E., & Pierpaoli, E. 2011, *ApJ*, **737**, 98
- Planck Collaboration 2013, Planck explanatory supplement, First release v1.00
- Planck Collaboration 2014a, *A&A*, **571**, 1
- Planck Collaboration 2014b, *A&A*, **571**, 2
- Planck Collaboration 2014c, *A&A*, **571**, 11
- Planck Collaboration 2014d, *A&A*, **571**, 12
- Planck Collaboration 2014e, *A&A*, **571**, 13
- Planck Collaboration 2014f, *A&A*, **571**, 27
- Planck Collaboration 2014g, *A&A*, **561**, 97
- Rathaus, B., Kovetz, E. D., & Itzhaky, N. 2013, *MNRAS*, **431**, 3678
- Rubert, M., Bacon, D., & Schwarz, D. J. 2014, *A&A*, **565**, 111
- Strauss, M. A., & Willick, J. A. 1995, *PhR*, **261**, 271
- Sunyaev, R. A., & Zel'dovich, Y. B. 1970, *ApSS*, **7**, 3
- Sunyaev, R. A., & Zel'dovich, Y. B. 1972, *CoASP*, **4**, 173
- Turnbull, S. J., Hudson, M. J., Feldman, H. A., et al. 2012, *MNRAS*, **420**, 447
- Turner, M. S. 1991, *PhRv*, **44**, 3737
- Watkins, R., & Feldman, H. A. 2014, *MNRAS*, **447**, 132
- Watkins, R., Feldman, H. A., & Hudson, M. J. 2009, *MNRAS*, **392**, 743
- Wiltshire, D., Smales, P., Mattsson, T., & Watkins, R. 2013, *PhRvD*, **88**, 3529